CHEMISTRY OF MATERIALS

ARTICLE

pubs.acs.org/cm

Probing the Chemical Stability of Mixed Ferrites: Implications for Magnetic Resonance Contrast Agent Design

Elise A. Schultz-Sikma,[†,§] Hrushikesh M. Joshi,[‡,§] Qing Ma,[⊥] Keith W. MacRenaris,[†] Amanda L. Eckermann,[†] Vinayak P. Dravid,[‡] and Thomas J. Meade*[,†,¶]

[†]Department of Chemistry and [‡]Department of Materials Science and Engineering, Northwestern University, Evanston, Illinois 60208, United States

[⊥]DND-CAT, Argonne National Laboratory Synchrotron Research Center, Northwestern University, Argonne, Illinois 60439, United States

Supporting Information

ABSTRACT: Nanomaterials with mixed composition, in particular magnetic spinel ferrites, are emerging as efficient contrast agents for magnetic resonance imaging. Many factors, including size, composition, atomic structure, and surface properties, are crucial in the design of such nanoparticle-based probes because of their influence on the magnetic properties. Silica-coated iron oxide (IO-SiO_2) and cobalt ferrite (CoIO-SiO_2) nanoparticles were synthesized using standard high-temperature thermal decomposition and base-catalyzed water-in-oil microemulsion techniques. Under neutral aqueous conditions, it was found that 50−75% of the cobalt content in the CoIO-SiO_2 nanoparticles leached out of the core structure. Leaching caused a 7.2-fold increase in the longitudinal relaxivity and an increase in the saturation magnetization from ∼48 to ∼65 emu/g of the core. X-ray absorption fine structure studies confirmed that the atomic structure of the ferrite core was altered following leaching, while transmission electron microscopy and dynamic light scattering confirmed that the morphology and size of the nanoparticle remained unchanged. The CoIO-SiO_2 nanoparticles converted from a partially inverted spinel cation arrangement (unleached state) to an inverse spinel arrangement (leached state). The control IO-SiO_2 nanoparticles remained stable with no change in the structure and negligible changes in the magnetic behavior. This detailed analysis highlights how important understanding the properties of nanomaterials is in the development of reliable agents for diagnostic and therapeutic applications.

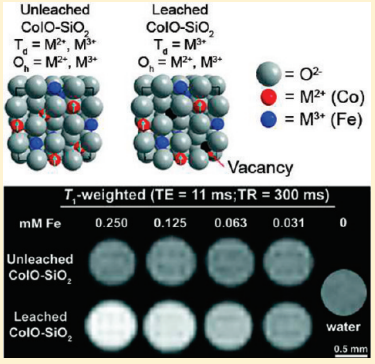

KEYWORDS: MRI, ferrite, nanoparticle, leaching, magnetic properties

INTRODUCTION

Magnetic spinel ferrites ($M_xFe_{3-x}O_4$, where M = Fe, Co, Mn, Ni, or Zn) have emerged as versatile nanomaterials for use in numerous biological applications, such as thermal activation therapy, biosensing, drug delivery, and magnetic resonance imaging (MRI).[1−7] Superparamagnetism coupled with tunable surface properties renders these structures particularly valuable as contrast agents for MRI. Among the ferrites, Fe_3O_4 (iron oxide, IO) nanoparticles have been the most widely used particle-based MRI contrast agents.[8−13] However, advances in synthetic techniques that allow control over morphology and composition have made mixed-metal ferrites, such as cobalt ferrite ($CoFe_2O_4$) and manganese ferrite ($MnFe_2O_4$), promising additions to the development of nanoparticle probes with tunable magnetism and MRI contrast effects.[2,14−16] Cobalt ferrite, in particular, has received substantial attention for its theranostic potential (MRI and thermal activation) due to its unique magnetic properties, such as large anisotropy energy, tunable coercivity, and high saturation magnetization.[1,17−19]

Superparamagnetic (SPM) ferrite nanoparticles are powerful MRI contrast agents because of their large magnetic moments, which result from the cooperativity of the individual spins when aligned in the presence of an external magnetic field.[20] This high magnetic susceptibility creates local magnetic field inhomogeneities, which appreciably shorten the T_2 and T_2^* relaxation times (dephasing) of nearby water protons and produces a darker intensity in a magnetic resonance image.[21] Relaxivity is a measure of the effectiveness of a contrast agent at manipulating the relaxation times (T_1 and T_2) of proton spins.[22] The higher the relaxivity, the more efficient the material is as an MRI contrast agent. Superconducting quantum interference device (SQUID) magnetometry is used to further assess the magnetic properties of SPM nanoparticles by measuring the magnetic susceptibility (χ) and saturation magnetization (M_s) of the material.

Optimization of the magnetic properties, stability, and in vivo biocompatibility is at the forefront in the design of our nanoparticle MRI contrast agents.[23−27] These properties depend on many factors, including the particle size, crystallinity, composition, crystallographic structure (cation distribution), surface morphology, and surface coating.[4,18,28−30] Particularly, the effects of the size and composition on the magnetic properties of ferrite nanoparticles have been thoroughly investigated.[14,31−33]

Received: February 17, 2011
Published: April 25, 2011

It was determined that, as the nanoparticle size increases, the magnetic properties (magnetization and relaxivity) are enhanced. Furthermore, the doping of magnetic atoms (e.g., Mn^{2+}, Co^{2+}, and Ni^{2+}) into the Fe_3O_4 structure leads to a decrease in the magnetic properties following the trend Mn > Fe > Co > Ni.

An extensive amount of research has been focused on learning how changes in the structure, cation distribution, and surface properties affect the magnetic properties of a material.[34−38] Bulk ferrites adopt a spinel arrangement of metal cations with cubic symmetry that contains 32 oxygen atoms, 16 trivalent metal ions, and 8 divalent metal ions.[18,39] In a normal spinel arrangement, the divalent cations occupy tetrahedral (T_d) crystallographic sites and the trivalent cations reside in octahedral (O_h) sites. Magnetic ferrites (e.g., Fe_3O_4, $CoFe_2O_4$, and $MnFe_2O_4$) are expected to have an inverse spinel arrangement, where the 16 trivalent cations are split between the T_d and O_h sites and the 8 divalent cations occupy the remaining O_h sites. The distribution of the cations among the two types of crystallographic sites depends on the radii, electronic structure, and valence of the metal ions in the ferrite.[34,38,40] Bulk Fe_3O_4 is known to have a pure inverse spinel arrangement; however, it has been found that mixed ferrites, such as $CoFe_2O_4$ and $MnFe_2O_4$, often have a partially inverted spinel structure (in between normal and inverse).[34] On the nanoscale, the preparation conditions, namely, the M^{2+}/Fe^{2+} ratio in the precursor solution and temperature, influence the resulting cation distribution (core structure) and magnetic properties of the nanoparticle product.[36,40]

X-ray diffraction (XRD), Mössbauer spectroscopy, and X-ray absorption fine structure (XAFS) are each useful methods for obtaining structural information. However, XAFS techniques, which include X-ray absorption near edge structure (XANES) and extended XAFS (EXAFS), are highly sensitive for studying the atomic structure of multicomponent, dilute, and disordered systems on the nanoscale.[34,41] XANES provides information on the site symmetry and oxidation state of the absorbing atom in the material. EXAFS reveals the atomic coordination around the absorbing atom, including information on the bond distances and coordination numbers.

The surface of the nanoparticle core can have an important effect on the structure and magnetic properties of the material. When the particle size is decreased into the nanoregime, the properties of the material are altered as the surface area becomes very large in comparison to the bulk state. The electron spins on the surface of a magnetic material are canted (or disordered) because of reduced spin−spin exchange near the surface.[2] In bulk material, the canted surface is minimal compared to the large volume, but the effect of the canting is a great deal more prominent for nanomaterials having high surface area-to-volume ratios. Because of this large surface area, more metal cations are located near the surface.[40] Changes in the cation distribution of the metal ions will inevitably alter the morphology of the surface layer and, in turn, the magnetic properties of the nanoparticle. The role of the surface morphology on the properties of the material is further complicated by the coating surrounding the magnetic core. Ferrite nanoparticles require surfactants or coatings to prevent aggregation when in aqueous media and to afford biocompatible, stable MRI contrast agents. These coatings are typically organic ligands, small-molecule charge stabilizers, polymers, and inorganic materials.[3,4,21,28,32,42] The nature of the coating will affect water access to the magnetic core, thereby influencing the relaxivity and efficacy of the agent.

In the design and evaluation of mixed ferrite nanoparticles as viable MRI probes, the chemical stability is one of the most critical parameters to consider. The nanoparticle and its properties need to remain constant in order to have an effective probe. There is some literature precedence for the release of metal ions from ferrite nanoparticles, specifically $CoFe_2O_4$. Soler et al. studied the influence of surface passivation on the aging of $CoFe_2O_4$ in highly acidic media (pH < 2).[43] In all of the aged samples, dissolution of $CoFe_2O_4$ was observed (up to 50%), affecting the structure, cation distribution, and magnetization of the nanoparticles. Baldi et al. demonstrated the impact of surface coating on the leaching of cobalt ions from $CoFe_2O_4$ nanoparticles.[44] They found that the nature of the surface coating influenced the extent of cobalt release at neutral pH. While these studies confirmed the leaching of metal ions from $CoFe_2O_4$ nanoparticles, the experimental conditions were not biologically relevant or the effect of leaching on the structural and magnetic properties was not investigated.

Here, we present a detailed analysis of the chemical stability of silica-coated $CoFe_2O_4$ core−shell nanoparticles in solution for use as MRI contrast agents. We describe the leaching process of metal ions from the core and its direct impact on the structural and magnetic integrity of the nanoparticles. Typically, structural and magnetic investigations of ferrites have been performed on powder samples, and changes in the chemical composition are deliberate and imposed by the synthetic conditions.[34,36,37,40,45−48] We find that significant changes in the chemical composition of these $CoFe_2O_4$ nanoparticles occur *spontaneously* during dialysis in an aqueous solution without the use of harsh reagents or pH conditions. The leaching of metal ions alters the crystal structure of the nanoparticle core, significantly affecting the magnetic properties. The magnetism and structure of the nanoparticles in this study were characterized by magnetometry, relaxometry, and XAFS analysis and compared to control Fe_3O_4 nanoparticles. Such detailed, localized analysis of nanocomposites is imperative to understanding their properties and behavior to ultimately develop reliable carriers for diagnostic and therapeutic applications.

MATERIALS AND METHODS

All chemicals and reagents were purchased from Sigma Aldrich (St. Louis, MO) and used without further purification. XAFS reference compounds of the highest purity available were purchased from Alfa Aesar (Ward Hill, MA) and used as received. Regenerated cellulose 12−14 000 molecular weight cutoff (MWCO) Spectra/Por 4 membrane tubing was purchased from Spectrum Laboratories, Inc. (Rancho Dominguez, CA). Amicon Ultra-4 100 000 MWCO centrifugal filter units were purchased from Millipore (Billerica, MA). Elemental inductively coupled plasma (ICP) standards for Fe and Co were purchased from Sigma Aldrich (St. Louis, MO). Multielement internal standard (10 μg/mL Bi, Ho, In, Li, Sc, Tb, and Y in 2% nitric acid) was purchased from Spex Certiprep Inc. (Metuchen, NJ). Water was purified using a Millipore Milli-Q Synthesis water system (Billerica, MA).

Nanoparticle Synthesis: Core Formation. $CoFe_2O_4$ cores were prepared using a previously published procedure.[1] Briefly, iron(III) acetylacetonate (4 mmol) and cobalt(III) acetylacetonate (2 mmol) were dissolved in 40 mL of benzyl ether. The surfactants dodecylamine (12 mmol), lauric acid (12 mmol), and 1,2-hexadecanediol (20 mmol) were added to reduce and stabilize the nanoparticle surface. The solution was heated to 200 °C for 30 min under a nitrogen atmosphere and then raised to 280 °C for 30 min. The nanoparticles were precipitated with ethanol, followed by magnetic separation. Fe_3O_4 cores were synthesized

by the same procedure using an iron(III) acetylacetonate precursor (2 mmol), 6 mmol of dodecylamine, 6 mmol of lauric acid, and 10 mmol of 1,2-hexadecanediol in 20 mL of benzyl ether.

Nanoparticle Synthesis: Silica Shell Formation. Silica (SiO_2) was used to coat the core by a base-catalyzed water-in-oil micoremulsion approach with slight modification from a previously published procedure.[59] Igepal CO-520 (1 mL) was mixed with anhydrous cyclohexane (20 mL) and stirred for 10 min. The nanoparticle cores were dispersed in cyclohexane at a concentration of 1 mg/mL and slowly added to the Igepal CO-520/cyclohexane emulsion. An aqueous solution of 30% NH_4OH (0.140 mL) was added dropwise and stirred for 15 min, followed by the addition of tetraethylorthosilicate (0.170 mL). The mixture was stirred for 48 h before the addition of ethanol to precipitate the core−shell nanoparticles. The precipitate was collected by centrifugation, and the nanoparticles were washed by redispersion in ethanol. The nanoparticles were washed at least three times to remove excess surfactant. The final product was dispersed directly in water.

Metal Ion Leaching Experiments. Nanoparticles (0.5 mL of ∼1 mg/mL) were leached by extensive dialysis against approximately 20 L of water for 2−3 days using 12−14 000 MWCO regenerated cellulose membranes. After dialysis, the leached nanoparticles were concentrated by size filtration using Amicon Ultra-4 100 000 MWCO centrifugal filter devices. The nanoparticles were washed three times with water in the centrifugal filter units. The resulting leached nanoparticle stock solutions were adjusted with water to a final volume of 0.5 mL, and brief ultrasonication was used to fully disperse the nanoparticles.

Transmission Electron Microscopy (TEM). TEM images were obtained at room temperature on a Hitachi HF-8100 instrument operated at 200 kV using the imaging mode (Pleasanton, CA). The nanoparticle diameters were determined by statistical averaging using a digital micrograph. All TEM samples were prepared by directly transferring and evaporating the nanoparticle suspension onto a standard copper grid coated with a carbon film under ambient conditions.

XRD. XRD measurements were performed on a powder sample of $CoFe_2O_4$ core structures using a Rigaku goniometer. The instrument was equipped with a long, fine-focus copper X-ray tube (λ = 0.154 06 nm) and operated at 40 kV and 20 mA with 1° divergent and antiscattering slits coupled with 0.1 mm receiving slits. The scan was performed with 2θ steps of 0.05°/step, and the collection time was 2 s for each point. The XRD patterns for Fe_3O_4 cores were collected on a Scintag X-ray machine with similar settings (except for a step size of 0.1°/step). XRD analysis was performed in the J. B. Cohen X-ray Diffraction Facility at Northwestern University (Evanston, IL).

Dynamic Light Scattering (DLS). The hydrodynamic size was determined using DLS on a Malvern Instruments Zetasizer Nano Series Nano-ZS with Dispersion Technology Software 5.03 (Worcestershire, U.K.). Samples were measured in an aqueous solution using polystyrene cuvettes with a 10 mm optical pathway at 25 °C. Each sample was measured at a concentration of 0.25 mM Fe. A total of 15 scans were performed per sample, and the results were averaged. The data were obtained as log-normal distribution plots. Intensity-, volume-, and number-weighted size distributions were analyzed; however, only number-weighted values are reported.

Inductively Coupled Plasma Mass Spectrometry (ICP-MS). Element concentrations were determined using a Thermo Electron Corporation XSeries^{II} inductively coupled plasma mass spectrometer with Thermo PlasmaLab software (Waltham, MA). The instrument was operated in collision cell technology mode. Samples for ICP analysis were digested in 70% *Trace*SELECT nitric acid at 65 °C for ∼3 h and diluted to 3% (v/v) nitric acid. Fe and Co standards were prepared in 3% (v/v) nitric acid with concentrations of 0.5, 1, 5, 15, 50, 125, and 250 ng/mL. A multielement internal standard (containing 10 μg/mL Bi, Ho, In, Li, Sc, Tb, and Y) was added to each standard and sample to yield a final concentration of 5 ng/mL. Isotopes ^{57}Fe and ^{59}Co were used for determination of the element concentration. Isotopes ^{45}Sc, ^{89}Y, ^{115}In, and ^{165}Ho were used as internal standards.

Magnetic Susceptibility. Magnetic susceptibility measurements were carried out on a Quantum Design MPMS5 SQUID magnetometer (San Diego, CA). Samples were dispersed in water and frozen under a nitrogen environment. The magnetization (M), as a function of the applied magnetic field (H), was acquired at 260 K over fields between −50 and +50 kOe. From the hysteresis loops (M vs H plots), coercivity, remanence, and saturation magnetization (M_s) were obtained. M_s was determined by plotting M vs $1/H$ at high fields and extrapolating to $1/H = 0$. All SQUID data were corrected for diamagnetism by subtracting the diamagnetic contribution at high fields near magnetic saturation.

Relaxometry. Longitudinal (T_1) and transverse (T_2) relaxation times were measured at 60 MHz and 37 °C on a Bruker mq60 NMR analyzer equipped with The Minispec V2.51 Rev.00/NT software (Billerica, MA). Each sample was diluted with water to make five concentrations (0.0625−1 mM Fe). An inversion−recovery pulse sequence was used to measure the T_1 relaxation times, while a spin−echo pulse sequence was used to measure transverse T_2 relaxation times. The initial and final pulse separations were adjusted to obtain the best monoexponential curve fit. Relaxation times were determined using monoexponential curve fitting of 10 data points (four averages for each point). The relaxivity was determined by taking the slope of a plot of $1/T_n$ (n = 1, 2) versus concentration (mM Fe).

Magnetic Resonance Phantom Imaging and Analysis at 7 T. 7 T MRI and T_1/T_2 measurements were performed on a Bruker PharmaScan 7 T horizontal, wide-bore (89 mm) imager (Bruker, Billerica, MA) fitted with shielded gradient coils at 25 °C. For solution phantom images, 25 μL solutions containing leached or unleached cobalt ferrite core-shell nanoparticles (0.25, 0.125, 0.0625, and 0.03125 mM Fe) in water were each added to a flame-sealed 9-in. Pasteur pipet. The bottom of the flame-sealed pipet was then scored with a glass scribe and broken into small capillaries, their tops were wrapped in Parafilm to avoid sample evaporation, and they were then imaged in a transmit/receive 23-mm mouse-head coil.

Spin−lattice relaxation times (T_1) were measured using a rapid acquisition rapid echo (RARE)−T_1 map pulse sequence, with static TE (11 ms) and variable TR (117, 200, 300, 500, 750, 1000, 1500, 3000, 6000, 8000, 10 000, and 15 000 ms) values. Imaging parameters were as follows: field of view (FOV) = 25 × 25 mm^2, matrix size (MTX) = 256 × 256, number of axial slices = 4, slice thickness = 1.0 mm, and averages (NEX) = 3. T_1 analysis was carried out using the image sequence analysis tool in Paravision 5.0 pl3 software (Bruker, Billerica, MA) with monoexponential curve fitting of the image intensities of selected regions of interest (ROIs) for each axial slice.

Spin−spin relaxation times (T_2) were measured using a multislice multiecho (MSME)−T_2 map pulse sequence, with static TR (6000 ms) and 32 fitted echoes in 11 ms intervals (11, 22, ..., 352 ms). Imaging parameters were as follows: FOV = 25 × 25 mm^2, MTX = 256 × 256, number of axial slices = 4, slice thickness = 1.0 mm, and NEX = 3. T_2 analysis was carried out using the image sequence analysis tool in Paravision 5.0 pl3 software (Bruker, Billerica, MA) with monoexponential curve fitting of the image intensities of selected ROIs for each axial slice.

XAFS. XAFS experiments were carried out at the bending magnet beamline (5-BM-D) operated by DND-CAT at the Advanced Photon Source of Argonne National Laboratory (Argonne, IL). The beamline uses a Si(111) monochromator for energy selection. The energy resolution at the Fe K-edge (7112 eV) is ∼1.0 eV. During the X-ray absorption measurements, the synchrotron storage ring was operated in the "top-up" mode, with the electron beam current kept at ∼100 mA. The X-ray beam size in the experimental station is selected by two sets of Huber slits that are 2 × 8 mm^2. The X-ray energies are calibrated by using Fe and Co standards for the measurements carried out at each K absorption edge, respectively. In addition to these, a series of oxide

Scheme 1. Synthesis of IO-SiO_2 and CoIO-SiO_2 Core−Shell Nanoparticles[a]

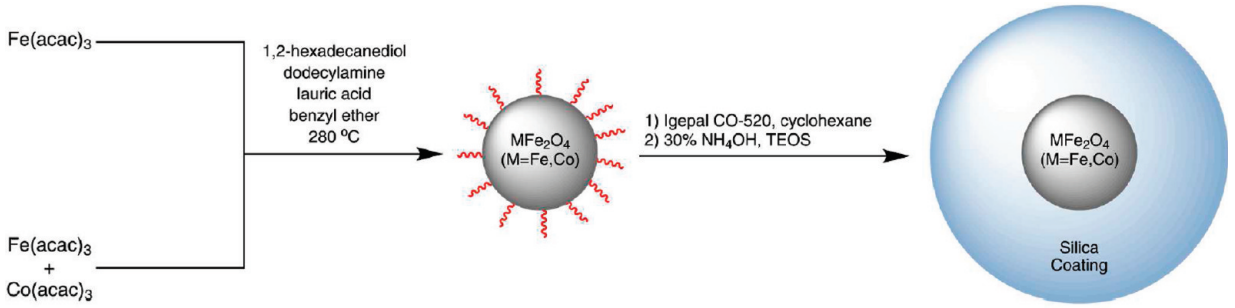

[a] The red coating represents organic-capping ligands (dodecylamine and lauric acid) on the core surface.

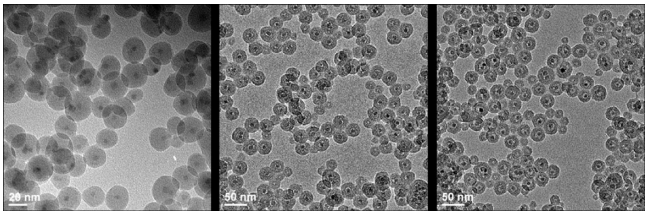

Figure 1. TEM images of IO-SiO_2 (left), unleached CoIO-SiO_2 (center), and leached CoIO-SiO_2 (right) nanoparticles. Note the uniform coating around the nanoparticle core, which is retained following the leaching process.

powder samples, Fe_3O_4, γ-Fe_2O_3, $CoFe_2O_4$, CoO, and Co_3O_4, were measured in the transmission mode at room temperature.

The incident X-ray intensity was monitored by an ion chamber (Oxford Danfysik). A 13-element Ge solid-state detector (Canberra) was used to collect the fluorescence emissions of Fe and Co Kα to obtain XANES and EXAFS spectra at room temperature. The samples were oriented 45° to the incident X-ray and to the 13-element detector. The digital X-ray process electronics (DXP2X) from the X-ray instrument associate are used for X-ray pulse processing, which provides precise dead-time correction within a given experimental condition. Typically, 5−10 energy scans were averaged to obtain sufficiently good data statistics. The XANES spectra allow determination of the chemical states of the absorbing atoms and the symmetry of the nearest coordination. The EXAFS spectra reveal the interatomic distances (R), the root mean squares of the bond distance spread (or the Debye−Waller factor, σ^2), and the coordination numbers (N) around each absorbing atom.[41]

The X-ray absorption data analyses were carried out using the *ATHENA* software package.[49] The EXAFS phases and amplitudes were all generated using the FEFF8 code that is embedded in the *ATHENA* package. The intrinsic loss parameter (S_0^2) for various absorbing atoms, which is taken as a constant (independent of photoelectron kinetic energies), was determined using the reference materials. The EXAFS data of Fe_3O_4 and its crystallographic structure were used to extract the S_0^2 value for the Fe K-edge data. Fe_3O_4 belongs to the cubic space group $Fd\bar{3}m$ with lattice constant a = 8.391 Å and α = 90°. The EXAFS data for Co_3O_4 and its crystallographic structure were used to extract the S_0^2 value for the Co K-edge data. Co_3O_4 belongs to the cubic space group $Fd\bar{3}m$ with lattice constant a = 8.084 Å and α = 90°.

Reference compounds were used in powder form. Samples were ground to make a fine powder and spread on a piece of Scotch tape to a suitable, highly uniform density, and the tape was layered to increase the optical thickness. Nanoparticle samples were measured as aqueous solutions. The stable solutions were loaded into a polypropylene sample holder sealed with Kapton tape.

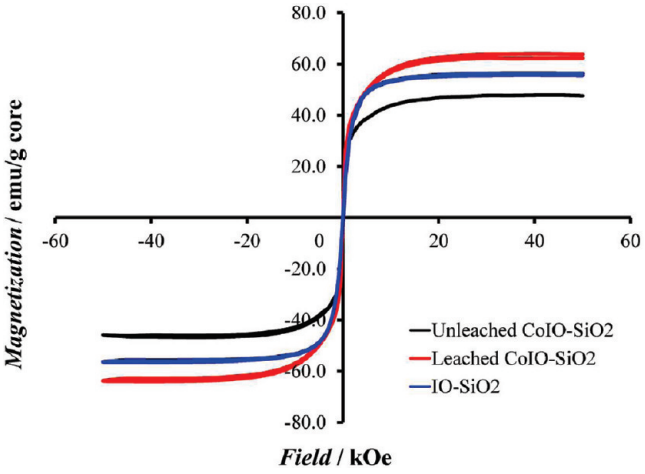

Figure 2. Hysteresis loops at 260 K measured using SQUID magnetometry. The curves show the SPM behavior and M_s of the core−shell nanoparticles: IO-SiO_2 (blue), unleached CoIO-SiO_2 (black), and leached CoIO-SiO_2 (red).

RESULTS AND DISCUSSION

Ferrite cores, Fe_3O_4 (IO) and $CoFe_2O_4$ (CoIO), were synthesized using a high-temperature solution decomposition method followed by silica (SiO_2) coating using a base-catalyzed water-in-oil microemulsion approach to produce aqueous-dispersed nanoparticles (IO-SiO_2 and CoIO-SiO_2; Scheme 1). Silica was chosen based on its hydrophilicity and established chemistry for surface modification.[50−52] The uniform shape and monodispersity of the nanoparticles were confirmed by TEM analysis (Figure 1). The average size of the cores is 7 ± 1 nm, with a SiO_2 shell thickness of approximately 10 nm. In solution, the nanoparticles have hydrodynamic sizes of 70 ± 9 nm for IO-SiO_2 and 52 ± 19 nm for CoIO-SiO_2. The SiO_2-coated nanoparticles exhibit core−shell morphology with long-term colloidal stability in aqueous media. XRD measurements verified formation of the ferrite phase for both nanoparticle compositions (Figure S1 in the Supporting Information).

Exposing aqueous solutions of the CoIO-SiO_2 nanoparticles (0.33−0.50 Co/Fe ratio) to dialysis produced a *significant* change in the core composition. Elemental analysis of the nanoparticles revealed that 50−75% of the Co ions consistently leach out of the ferrite structure. The core composition reaches equilibrium at approximately 12−16% Co (0.12−0.16 Co/Fe

dx.doi.org/10.1021/cm200509g |*Chem. Mater.* 2011, 23, 2657–2664

ratio). The high degree of leaching associated with these nanoparticles is surprising given that silica has been shown to be a robust coating for metal-based materials by protecting against degradation and preventing the release of toxic metallic species.[53−55] TEM and DLS analysis showed that the size and distribution of the nanoparticles did not change following the leaching process (Figures 1 and S2 in the Supporting Information).

The magnetic susceptibility of the nanoparticles was measured using SQUID magnetometry. Isothermal hysteresis loops were collected at 260 K (Figure 2). The SPM nature of the nanoparticles at this temperature is reflected in the negligible coercivity and remanence (Figure 2 and Table S1 in the Supporting Information). CoIO-SiO_2 nanoparticles exhibited a large increase in the saturation magnetization (M_s) between the unleached and leached states (48.4 and 64.9 emu/g of the core, respectively). M_s of the control IO-SiO_2 nanoparticles was 56.9 emu/g of the core.

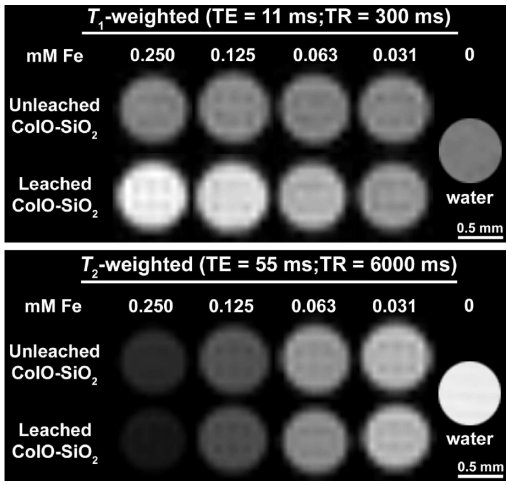

Figure 3. Magnetic resonance images of solution phantoms of unleached and leached CoIO-SiO_2 nanoparticles at different iron concentrations (0.031−0.25 mM Fe) at 7 T and 25 °C. T_1-weighted (RARE−T_1 map) and T_2-weighted (MSME−T_2 map) images were acquired using the following parameters: FOV = 25 × 25 mm^2, MTX = 256 × 256, axial slices = 4, slice thickness = 1.0 mm, NEX = 3.

Considering the influence of leaching on the core magnetization of CoIO-SiO_2, the relaxivity of the nanoparticles was evaluated at 60 MHz and 37 °C to determine if there was an analogous effect. Prior to leaching, CoIO-SiO_2 and IO-SiO_2 nanoparticles exhibit similar spin−lattice relaxivity (r_1) values (3.0 mM^{-1} s^{-1} Fe and 2.7 mM^{-1} s^{-1} Fe, respectively). However, CoIO-SiO_2 nanoparticles have a higher spin−spin relaxivity (r_2) than IO-SiO_2 (113 mM^{-1} s^{-1} Fe vs 82.2 mM^{-1} s^{-1} Fe). Following leaching, a substantial increase in r_1 is observed for CoIO-SiO_2 (21.5 mM^{-1} s^{-1} Fe), representing a 7.2-fold improvement. IO-SiO_2 nanoparticles were dialyzed as a control and showed a 1.5-fold higher r_1 postleaching (4.1 mM^{-1} s^{-1} Fe). With respect to r_2, there is only a 1.2-fold increase postleaching for both CoIO-SiO_2 and IO-SiO_2 (142 mM^{-1} s^{-1} Fe and 97.6 mM^{-1} s^{-1} Fe, respectively). In comparison, Ferumoxytol (a commercial nanoparticle) has a relaxivity of 17.5 mM^{-1} s^{-1} Fe for r_1 and 63.3 mM^{-1} s^{-1} Fe for r_2.

The effect of leaching on the relaxivity of CoIO-SiO_2 is partly attributed to the change in M_s. The enhancement in M_s of the leached nanoparticles, and the subsequent increase in the relaxivity, renders these nanoparticles more effective MRI agents. The contrast enhancement afforded by leaching of CoIO-SiO_2 was detectable by MRI at 7 T (298 MHz). The overall magnitude of r_1 decreases at this higher field strength; however, the leached nanoparticles clearly show brighter contrast in T_1-weighted images compared to the unleached counterparts (Figure 3 and

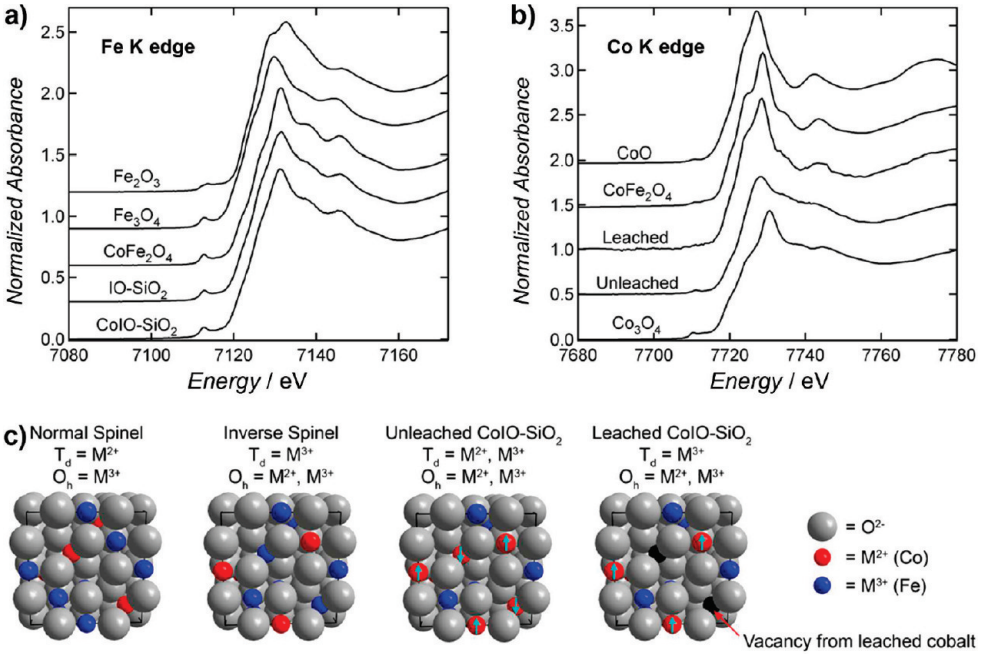

Figure 4. Fe K-edge (a) and Co K-edge (b) XANES spectra for core−shell nanoparticles (IO-SiO_2 and unleached and leached CoIO-SiO_2) and reference oxides (Fe_2O_3, Fe_3O_4, $CoFe_2O_4$, CoO, and Co_3O_4). (c) Crystallographic model of lattice changes imposed by leaching. Structural analysis revealed that the leaching process removed T_d-coordinated Co ions from the nanoparticle core, resulting in a transition from the partially inverted structure (unleached) to the inverse spinel structure (leached).

dx.doi.org/10.1021/cm200509g |*Chem. Mater.* 2011, 23, 2657–2664

the Supporting Information). The leached and unleached nanoparticles were not as distinguishable in the T_2-weighted images.

To determine if the observed changes in the magnetic properties following leaching can be correlated to structural changes in the nanoparticle, XAFS was employed. Figure 4a shows the Fe K-edge XANES of IO-SiO_2 and CoIO-SiO_2 compared to Fe-based reference compounds. The nanoparticles clearly resemble the $CoFe_2O_4$ and Fe_3O_4 reference oxides. The cation arrangement of these reference bulk oxides is inverse spinel, where Fe^{3+} ions occupy all of the tetrahedral (T_d) crystallographic sites and half of the octahedral (O_h) sites and Fe^{2+} (or Co^{2+}) ions occupy the remaining O_h sites. The preedge peak at ~7112 eV is due to the 1s → 3d transition, which is only allowed in the absence of inversion symmetry, as in the case of T_d site occupancy. The similarity of the XANES spectra of the nanoparticles to the references Fe_3O_4 and $CoFe_2O_4$ supports the fact that the Fe atoms in IO-SiO_2 and CoIO-SiO_2 favor the inverse spinel arrangement. Importantly, no apparent structural changes in the local environment of the Fe atoms were observed in the nanoparticles following leaching (see Figure S5 in the Supporting Information).

Figure 4b compares the Co K-edge XANES spectra of unleached and leached CoIO-SiO_2 nanoparticles with reference oxides CoO, Co_3O_4, and $CoFe_2O_4$. The XANES spectrum of the unleached CoIO-SiO_2 is distinctly different from those of the other samples, and the existence of a preedge peak, although weak, signifies that some of the Co ions are situated in T_d sites. Further, the Co K-edge data for the unleached sample resemble the Fe K-edge spectrum (Figure 4a), indicating that the unleached CoIO-SiO_2 nanoparticles have a partially inverted spinel structure (between normal and inverse cation arrangements). For the Co content observed in the unleached nanoparticles (Co/Fe ratio = ~0.5), this arrangement is consistent with the literature.[37]

Upon leaching, changes occur in the local Co structure of the nanoparticles, as indicated by the differences in the XANES spectra (Figure 4b). The near-edge structure around the Co ions is similar to that in bulk $CoFe_2O_4$. The negligible preedge peak of the leached nanoparticles indicates that the Co ions occupy slightly distorted O_h sites. Therefore, following leaching, the decrease in the Co content (50−75%) results in a completely inverted spinel arrangement, where Co occupies only O_h sites (Figure 4c). The T_d sites are not structurally stable for the Co (2+) ions to reside in and are thus removed by leaching. On the basis of the extent of cobalt leaching, it is probable that a fraction of the leached ions came from O_h-coordinated sites.

The EXAFS data corroborate the findings from XANES analysis. As shown in Figure 5a, the EXAFS oscillations measured after the Fe K-edge for the unleached CoIO-SiO_2 are well-aligned with bulk $CoFe_2O_4$. The same is true for leached nanoparticles (data not shown). Interestingly, the EXAFS oscillations measured past the Co K-edge for the unleached CoIO-SiO_2 have greater similarity to the Fe K-edge EXAFS than to the Co K-edge of bulk $CoFe_2O_4$, supporting occupancy of some Co ions in T_d sites. Fourier transforms of the EXAFS data validate that the average local structure around the Co ions closely resembles that of the Fe ions (Figure 5c, solid lines). In the leached nanoparticles, the Co K-edge EXAFS and Fourier transform are essentially identical with those of the $CoFe_2O_4$ reference, confirming O_h occupancy of the Co ions in the inverse spinel arrangement (Figure 5b,d).

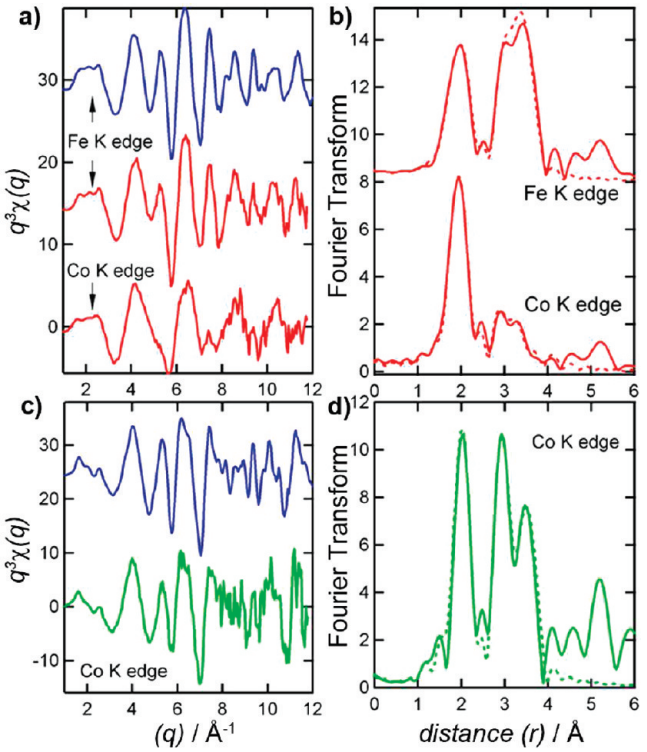

Figure 5. EXAFS spectra (a and b) and Fourier transforms (c and d) of the unleached (red) and leached (green) CoIO-SiO_2 nanoparticles. The EXAFS spectra of the reference $CoFe_2O_4$ (blue) are presented for comparison. The dashed lines are the fitting results obtained using the phases and amplitudes generated by the FEFF code based on the inverse spinel Fe_3O_4 structure. The unleached data are well described by a mixed-occupancy model (red dashes in part c), while the leached data are fitted by an O_h-occupancy model (green dashes in part d).

Quantitative analysis of the EXAFS data using the theoretical phases and amplitudes based on the inverse spinel Fe_3O_4 accurately simulates both Fe and Co K-edge EXAFS spectra for the unleached CoIO-SiO_2 sample (Figure 5c, dashed lines). The Fe−O bond distances are 1.85 Å (T_d site) and 1.99 Å (O_h site), comparing favorably to 1.86 and 2.03 Å found in the bulk Fe_3O_4 reference measured in this work. In the unleached nanoparticles, the Co−O bond distances are indistinguishable for the T_d and O_h sites (1.94 and 1.95 Å, respectively). For the leached sample, the theoretical simulation yields a Co−O bond distance of 2.04 Å for the nanoparticles versus 2.03 Å for bulk $CoFe_2O_4$ (Figure 5d, dashed line). The shorter Co−O bond distances in the unleached nanoparticles are consistent with a partially inverted structure, whereas the leached nanoparticles are representative of a pure inverse arrangement.[40,56]

The structural changes in the cation distribution and degree of inversion resulting from leaching account for the changes in the magnetic behavior observed here. According to the Néel model, magnetic ferrites, such as Fe_3O_4 and $CoFe_2O_4$, are ferrimagnetic and the alignment of their dipoles is governed by superexchange interaction.[18] The cations in T_d sites form one sublattice with their spins oriented in one direction, while the cations in O_h sites form a second sublattice with oppositely oriented spins. In these inverted spinels, the trivalent atoms in the T_d sublattice cancel those in the O_h sublattice, and the net magnetic moment is governed by the nature of the divalent atoms in the O_h sites. A partially inverted arrangement complicates the situation because

divalent atoms are present in both types of crystallographic sites. Here, the increased M_s after leaching is due, in part, to the removal of the T_d site Co^{2+}, which had previously compensated magnetically for some of the Co^{2+} ions in the O_h sublattice.

The leaching of Co ions creates vacancies in the nanoparticle core structure. As is evident from the relaxometry data, this has a more substantial effect on r_1 compared to r_2. For SPM nanoparticle contrast agents, outer-sphere interactions (diffusing bulk water in the local environment) are important in the T_1 relaxation process, and changes in the surface morphology can influence the interactions of bulk water with the nanoparticle, strongly affecting the relaxivity.[22,57] The vacancies created during the leaching process may distort the overall spinel structure, altering not only the magnetic properties but also the surface properties of the nanoparticle.[40,58] It is likely that the metal cations nearest the core surface are removed by leaching, which results in an increase in the surface area available to interact with water molecules. Because the silica coating should be porous and remains intact (Figure 1), we speculate that the large enhancement in r_1 is from these vacancies in the core, yielding greater accessibility of water to the surface.

CONCLUSIONS

The importance of investigating the chemical stability of nanoparticle composites was illustrated by a comprehensive characterization of the magnetic and structural properties of SiO_2-coated ferrite core−shell nanoparticles. Core−shell nanoparticles were successfully synthesized and exhibited long-term colloidal stability. The nanoparticles presented here were synthesized and purified with methods commonly employed in the making of nanoparticle-based MRI contrast agents. It was observed, however, that spontaneous leaching of Co ions from the nanoparticle core occurred under aqueous conditions without the addition of other reactants or changes in the pH. We have shown that leaching directly affects the saturation magnetization and relaxivity of CoIO-SiO_2 nanoparticles because of changes in the local structure and cation distribution of the nanoparticle core. The leaching of Co ions resulted in an improvement in the saturation magnetization and longitudinal relaxivity of the CoIO-SiO_2 nanoparticles. While a favorable effect, the significant differences in the magnetic behavior of the unleached and leached nanoparticles demonstrate how essential it is to carefully characterize such nanomaterials in solution. Further investigation is necessary to fully understand the driving force and mechanism of the leaching process. Additionally, there is still much that is unknown about nanomaterials and how they behave in vivo, which should not be further complicated by a lack of understanding of the properties of the agent itself. If ferrites and other nanomaterials of mixed composition are to become viable, efficient MRI contrast agents, then their chemical composition and magnetic properties must be maintained prior to biological studies.

ASSOCIATED CONTENT

Supporting Information. XRD spectra of Fe_3O_4 and $CoFe_2O_4$ nanoparticle cores, sample hydrodynamic size distributions obtained by DLS, quantitative data from SQUID measurements, additional 7 T MRI analysis and images, and additional XANES spectra. This material is available free of charge via the Internet at http://pubs.acs.org.

AUTHOR INFORMATION

Corresponding Author

*E-mail: tmeade@northwestern.edu.

Present Addresses

¶Present address: Departments of Chemistry, Biochemistry and Molecular Biology and Cell Biology, Neurobiology and Physiology, and Radiology, 2145 Sheridan Road, Evanston, IL 60208.

Author Contributions

§These authors contributed equally to this work.

ACKNOWLEDGMENT

The work performed at Northwestern University was supported by the Center for Cancer Nanotechnology Excellence (CCNE) initiative of the National Institutes of Health's National Cancer Institute under Award U54CA119341 and the National Institute of Biomedical Imaging and Bioengineering under Award 1RO1EB005866-01. The DND-CAT located at the Advanced Photon Source (APS) is supported by E. I. DuPont de Nemours & Co., The Dow Chemical Co., and the State of Illinois. Use of the APS was supported by the U.S. Department of Energy, Office of Science, Office of Basic Energy Sciences, under Contract DE-AC02-06CH11357. The SQUID measurements were performed by Oleksandr Chernyashevskyy in the Magnetic and Physical Properties Measurement Facility at Northwestern University. TEM analysis was performed in the EPIC/NIFTI facility of the NU*ANCE* Center at Northwestern University. Special thanks go to Collin Morris in the Chemistry Department at Northwestern University for help with the ferrite crystallographic models.

REFERENCES

(1) Joshi, H. M.; Lin, Y. P.; Aslam, M.; Prasad, P. V.; Schultz-Sikma, E. A.; Edelman, R.; Meade, T. J.; Dravid, V. P. *J. Phys. Chem. C* **2009**, *113*, 17761.

(2) Jun, Y.-W.; Seo, J.-W.; Cheon, J. *Acc. Chem. Res.* **2008**, *41*, 179.

(3) Hao, R.; Xing, R.; Xu, Z.; Hou, Y.; Gao, S.; Sun, S. *Adv. Mater.* **2010**, *22*, 2729.

(4) Laurent, S.; Forge, D.; Port, M.; Roch, A.; Robic, C.; Vander Elst, L.; Muller, R. N. *Chem. Rev.* **2008**, *108*, 2064.

(5) Jang, J.-t.; Nah, H.; Lee, J.-H.; Moon, S. H.; Kim, M. G.; Cheon, J. *Angew. Chem., Int. Ed.* **2009**, *48*, 1234.

(6) Pradhan, P.; Giri, J.; Samanta, G.; Sarma, H. D.; Mishra, K. P.; Bellare, J.; Banerjee, R.; Bahadur, D. *J. Biomed. Mater. Res., Part B* **2007**, *81B*, 12.

(7) Perez, J. M.; Simeone, F. J.; Saeki, Y.; Josephson, L.; Weissleder, R. *J. Am. Chem. Soc.* **2003**, *125*, 10192.

(8) Shen, T.; Weissleder, R.; Papisov, M.; Bogdanov, A., Jr.; Brady, T. J. *Magn. Reson. Med.* **1993**, *29*, 599.

(9) Josephson, L.; Tung, C.-H.; Moore, A.; Weissleder, R. *Bioconjugate Chem.* **1999**, *10*, 186.

(10) Amsalem, Y.; Mardor, Y.; Feinberg, M. S.; Landa, N.; Miller, L.; Daniels, D.; Ocherashvilli, A.; Holbova, R.; Yosef, O.; Barbash, I. M.; Leor, J. *Circulation* **2007**, *116*, I38.

(11) Bulte, J. W. M.; Kraitchman, D. L. *NMR Biomed.* **2004**, *17*, 484.

(12) Corot, C.; Robert, P.; Idee, J.-M.; Port, M. *Adv. Drug Delivery Rev.* **2006**, *58*, 1471.

(13) Gupta, A. K.; Naregalkar, R. R.; Vaidya, V. D.; Gupta, M. *Nanomedicine* **2007**, *2*, 23.

(14) Lee, J.-H.; Huh, Y.-M.; Jun, Y.-w.; Seo, J.-w.; Jang, J.-t.; Song, H.-T.; Kim, S.; Cho, E.-J.; Yoon, H.-G.; Suh, J.-S.; Cheon, J. *Nat. Med.* **2007**, *13*, 95.

(15) Sun, S.; Zeng, H.; Robinson, D. B.; Raoux, S.; Rice, P. M.; Wang, S. X.; Li, G. *J. Am. Chem. Soc.* **2004**, *126*, 273.
(16) Ammar, S.; Helfen, A.; Jouini, N.; Fiévet, F.; Rosenman, I.; Villain, F.; Molinie, P.; Danot, M. *J. Mater. Chem.* **2001**, *11*, 186.
(17) Franchini, M. C.; Baldi, G.; Bonacchi, D.; Gentili, D.; Giudetti, G.; Lascialfari, A.; Corti, M.; Marmorato, P.; Ponti, J.; Micotti, E.; Guerrini, U.; Sironi, L.; Gelosa, P.; Ravagli, C.; Ricci, A. *Small* **2010**, *6*, 366.
(18) Lax, B.; Button, K. J. *Microwave Ferrites and Ferrimagnetics*; McGraw-Hill Book Co., Inc.: New York, 1962.
(19) Ayyappan, S.; Mahadevan, S.; Chandramohan, P.; Srinivasan, M. P.; Philip, J.; Raj, B. *J. Phys. Chem. C* **2010**, *114*, 6334.
(20) Muller, R. N.; Roch, A.; Colet, J.-M.; Ouakssim, A.; Gillis, P. *The Chemistry of Contrast Agents in Medical Magnetic Resonance Imaging*; John Wiley & Sons, Ltd.: New York, 2001; p 417.
(21) Na, H. B.; Song, I. C.; Hyeon, T. *Adv. Mater.* **2009**, *21*, 2133.
(22) Månsson, S.; Bjørnerud, A. *The Chemistry of Contrast Agents in Medical Magnetic Resonance Imaging*; John Wiley & Sons, Ltd.: New York, 2001; p 1.
(23) Manus, L. M.; Mastarone, D. J.; Waters, E. A.; Zhang, X.-Q.; Schultz-Sikma, E. A.; MacRenaris, K. W.; Ho, D.; Meade, T. J. *Nano Lett.* **2010**, *10*, 484.
(24) Song, Y.; Xu, X.; MacRenaris, K. W.; Zhang, X.-Q.; Mirkin, C. A.; Meade, T. J. *Angew. Chem., Int. Ed.* **2009**, *48*, 9143.
(25) Hu, F.; Joshi, H. M.; Dravid, V. P.; Meade, T. J. *Nanoscale* **2010**, *2*, 1884.
(26) Hu, F.; MacRenaris, K. W.; Waters, E. A.; Liang, T.; Schultz-Sikma, E. A.; Eckermann, A. L.; Meade, T. J. *J. Phys. Chem. C* **2009**, *113*, 20855.
(27) Hu, F.; MacRenaris, K. W.; Waters, E. A.; Schultz-Sikma, E. A.; Eckermann, A. L.; Meade, T. J. *Chem. Commun.* **2010**, *46*, 73.
(28) Shubayev, V. I.; Pisanic, T. R., II; Jin, S. *Adv. Drug Delivery Rev.* **2009**, *61*, 467.
(29) Hamdeh, H. H.; Ho, J. C.; Oliver, S. A.; Willey, R. J.; Oliveri, G.; Busca, G. *J. Appl. Phys.* **1997**, *81*, 1851.
(30) Aslam, M.; Schultz, E. A.; Sun, T.; Meade, T. J.; Dravid, V. P. *Cryst. Growth Des.* **2007**, *7*, 471.
(31) Jun, Y.; Huh, Y.; Choi, J.; Lee, J.; Song, H.; Kim, S.; Yoon, S.; Kim, K.; Shin, J.; Suh, J.; Cheon, J. *J. Am. Chem. Soc.* **2005**, *127*, 5732.
(32) Duan, H.; Kuang, M.; Wang, X.; Wang, Y. A.; Mao, H.; Nie, S. *J. Phys. Chem. C* **2008**, *112*, 8127.
(33) Vestal, C. R.; Zhang, Z. J. *Int. J. Nanotechnol.* **2004**, *1*, 240.
(34) Carta, D.; Casula, M. F.; Falqui, A.; Loche, D.; Mountjoy, G.; Sangregorio, C.; Corrias, A. *J. Phys. Chem. C* **2009**, *113*, 8606.
(35) Lee, D. H.; Kim, H. S.; Lee, J. Y.; Yo, C. H.; Kim, K. H. *Solid State Commun.* **1995**, *96*, 445.
(36) Li, S.; Liu, L.; John, V. T.; O'Connor, C. J.; Harris, V. G. *IEEE Trans. Magn.* **2001**, *37*, 2350.
(37) Nakagomi, F.; da Silva, S. W.; Garg, V. K.; Oliveira, A. C.; Morais, P. C.; Franco, A.; Lima, E. C. D. *J. Appl. Phys.* **2007**, *101*, 09M514/1.
(38) Nakagomi, F.; da Silva, S. W.; Garg, V. K.; Oliveira, A. C.; Morais, P. C.; Franco, A., Jr. *J. Solid State Chem.* **2009**, *182*, 2423.
(39) Verwey, E. J. W.; Heilmann, E. L. *J. Chem. Phys.* **1947**, *15*, 174.
(40) Nordhei, C.; Ramstad, A. L.; Nicholson, D. G. *Phys. Chem. Chem. Phys.* **2008**, *10*, 1053.
(41) Rehr, J. J.; Albers, R. C. *Rev. Mod. Phys.* **2000**, *72*, 621.
(42) Pouliquen, D. *MML Series (Microspheres, Microcapsules, and Liposomes)*; Citus Books: London, U.K., 2001; Vol. 3, p 495.
(43) Soler, M. A. G.; Lima, E. C. D.; da Silva, S. W.; Melo, T. F. O.; Pimenta, A. C. M.; Sinnecker, J. P.; Azevedo, R. B.; Garg, V. K.; Oliveira, A. C.; Novak, M. A.; Morais, P. C. *Langmuir* **2007**, *23*, 9611.
(44) Baldi, G.; Bonacchi, D.; Franchini, M. C.; Gentili, D.; Lorenzi, G.; Ricci, A.; Ravagli, C. *Langmuir* **2007**, *23*, 4026.
(45) Jeyadevan, B.; Tohji, K.; Nakatsuka, K.; Narayanasamy, A. *J. Magn. Magn. Mater.* **2000**, *217*, 99.
(46) Li, S.; John, V. T.; O'Connor, C.; Harris, V.; Carpenter, E. *J. Appl. Phys.* **2000**, *87*, 6223.
(47) Zhou, Z.; Zhang, Y.; Wang, Z.; Wei, W.; Tang, W.; Shi, J.; Xiong, R. *Appl. Surf. Sci.* **2008**, *254*, 6972.
(48) Carta, D.; Mountjoy, G.; Navarra, G.; Casula, M. F.; Loche, D.; Marras, S.; Corrias, A. *J. Phys. Chem. C* **2007**, *111*, 6308.
(49) Ravel, B.; Newville, M. *J. Synchrotron Radiat.* **2005**, *12*, 537.
(50) Guerrero-Martínez, A.; Pérez-Juste, J.; Liz-Marzán, L. M. *Adv. Mater.* **2010**, *22*, 1182.
(51) Yi, D. K.; Lee, S. S.; Papaefthymiou, G. C.; Ying, J. Y. *Chem. Mater.* **2006**, *18*, 614.
(52) Parak, W. J.; Gerion, D.; Zanchet, D.; Woerz, A. S.; Pellegrino, T.; Micheel, C.; Williams, S. C.; Seitz, M.; Bruehl, R. E.; Bryant, Z.; Bustamante, C.; Bertozzi, C. R.; Alivisatos, A. P. *Chem. Mater.* **2002**, *14*, 2113.
(53) Durán, A.; Conde, A.; Gómez Coedo, A.; Dorado, T.; García, C.; Ceré, S. *J. Mater. Chem.* **2004**, *14*, 2282.
(54) Kirchner, C.; Liedl, T.; Kudera, S.; Pellegrino, T.; Javier, A. M.; Gaub, H. E.; Stölzle, S.; Fertig, N.; Parak, W. J. *Nano Lett.* **2005**, *5*, 331.
(55) Zhang, T.; Stilwell, J. L.; Gerion, D.; Ding, L.; Elboudwarej, O.; Cooke, P. A.; Gray, J. W.; Alivisatos, A. P.; Chen, F. F. *Nano Lett.* **2006**, *6*, 800.
(56) Harris, V. G.; Koon, N. C.; Williams, C. M.; Zhang, Q.; Abe, M.; Kirkland, J. P.; McKeown, D. A. *IEEE Trans. Magn.* **1995**, *31*, 3473.
(57) Tóth, E.; Helm, L.; Merbach, A. E. *The Chemistry of Contrast Agents in Medical Magnetic Resonance Imaging*; John Wiley & Sons, Ltd.: New York, 2001; p 45.
(58) Ogale, S. B. *Adv. Mater.* **2010**, *22*, 3125.
(59) Zhang, M.; Cushing, B. L.; O'Connor, C. J. *Nanotechnology* **2008**, *19*, 085601.